

Multiphysics Modeling to Assess the Powder Bed Characteristics of Inconel 718 for a Circular Substrate in Laser Powder Bed Fusion

Nayan Pundhir^{1*}, Oluwapelumi O. Adejumo¹, K. Chandrashekhara¹, and Joseph W. Newkirk²

¹Department of Mechanical and Aerospace Engineering

²Department of Nuclear Engineering

Missouri University of Science and Technology, Rolla, MO 65409

Heath Misak³ and Cesar O. Rios³

³Spirit AeroSystems, Wichita, KS 67210

Abstract

Laser powder bed fusion (LPBF) is a layer-by-layer additive manufacturing technique used to produce complex parts. In LPBF process, a laser directly melts and amalgamates metal powder particles. The quality of the manufactured part relies on several parameters, including the powder hatch space, packing fraction, laser power and scan speed. In this study, a computational fluid dynamics (CFD) model has been developed using FLOW-3D software. The powder bed characteristics of Inconel 718 have been evaluated for a single-layer, single-track deposition using the LPBF process on a circular substrate. The realistic powder size distribution data of Inconel 718 were obtained using scanning electron microscopy. The developed model has been used to predict the melt pool width and depth in order to optimize the process parameters. Additionally, the effect of airflow on powder erosion has been investigated to analyze particle displacement across the powder bed.

Keywords: LPBF, Inconel 718, Airflow, Particle size distribution

*Corresponding author: npwrt@mst.edu

Introduction

LPBF is one of the favorable additive manufacturing (AM) technologies. This technique has seen rapid adoption in the aerospace, energy, and medical sectors. In this process, a laser beam selectively melts regions of a metal powder bed layer by layer, following a predefined scanning strategy to build the final component [1]. Weiss et al. investigated how powder humidity affects LPBF processing and part quality across four metal powders (AlSi10Mg, Ti6Al4V, IN718, and 316L) with AlSi10Mg being the most sensitive to moisture [2].

The study examined how laser power and scan speed affect the surface quality of Ti6Al4V single tracks in LPBF, with scan speed emerging as the key contributor. Maintaining a fixed linear energy density, higher scan speeds and modified laser power lead to a significant reduction in the adhesion of partially fused powder particles during LPBF [3]. Inconel 718 is a nickel-based alloy strengthened through precipitation hardening, demonstrates excellent mechanical strength retention at temperatures as high as 650 °C [4].

Inconel 718 powder demonstrated the highest resistance to property degradation after repeated use in LPBF processes, with studies also showing that the flow properties of powder enhance with manifold uses [5]. This improved flow behavior helps ensure more uniform powder spreading and laser absorption, which supports stable part quality across builds. Increasing laser power and scan speed in LPBF, even at constant energy density, plays a role in determining the interface properties of Inconel 718 when deposited on wrought substrates. Laser power and scan speed aids in promoting the formation of a thicker melted interface zone, coarser grains, higher dendritic arm spacing, and increased porosity, including lack-of-fusion defects [6].

Machine learning models, particularly random forest and gradient boosted trees exhibit high precision in predicting the minimum creep rate of LPBF-fabricated Alloy 718 components. Key process parameters found to have the greatest impact include build orientation, laser count, and scan strategy. Porosity-related features, especially part density and number of pores showed a strong correlation with creep behavior [7]. Experimental and numerical studies on Inconel 718 LPBF builds showed that increasing interlayer temperatures in LPBF can alter melt pool morphology, leading to part deformation [8]. Pramod and Kesavan explored IN718 microstructure under varying volumetric energy density, combining finite element analysis and experiments to map conduction/keyhole regimes, highlighting post-heat treatment's role in relieving residual stress and improving mechanical strength [9].

In the present study, a multiphysics numerical model has been developed to simulate the LPBF process using IN718 powder. A single-layer, single-track melting scenario has been modeled using the weld module of FLOW-3D. The realistic particle size distribution of the IN718 powder, obtained through scanning electron microscopy (SEM) analysis, was incorporated into the model to accurately represent the powder bed. FLOW-3D POST was used to quantify the width and depth of the melt pool. Additionally, the effect of airflow on powder bed erosion was investigated to provide insights into particle displacement under varying flow conditions.

Numerical model

LPBF involves complex physical phenomena, including solidification, heat transfer, evaporation, and convection. To simplify these processes and enable the CFD model to effectively capture the underlying thermophysical behavior, the following assumptions are made: (a) powder particles are presumed to be spherical and randomly distributed on the substrate, (b) laser power absorptivity of the powder particles is considered constant, (c) specific heat and thermal conductivity are treated as temperature-dependent, and (d) the molten metal circulation is presumed to be incompressible, laminar, and Newtonian [10].

2.1. Discrete element method

Movement of powder particles in the LPBF process modeling has been predicted using Discrete Element Method (DEM). It enables the calculation of inter-particle forces and interactions with the surrounding environment during powder spreading [11]. Equation (1) shows the governing equation of translation motion and Equation (2) shows the rotational motion of individual particle.

$$m_i \frac{d^2 \mathbf{r}_i}{dt^2} = \sum_j (N_{ij} + T_{ij} + V_{ij}) + m_i g \quad (1)$$

$$I_i \frac{d\boldsymbol{\omega}_i}{dt} = \sum_j (Tr_{ij} + S_{ij}) \quad (2)$$

Where, m_i is mass of particle i , \mathbf{r}_i is position vector of particle i , N_{ij} is normal contact force, T_{ij} is tangential contact force, V_{ij} is van der Waals force exerted by particle j on particle i , and g is gravitational force. I_i is moment of inertia, $\boldsymbol{\omega}_i$ is angular velocity vector, Tr_{ij} is torque, and S_{ij} is sliding friction force.

2.2. Conservation equations

The partial differential equations depicting the conservation of mass, energy, and momentum are presented by Equations (3–5). These equations are solved simultaneously to predict fluid flow, pressure distribution, and velocity fields in the melt pool. Equation (3) represents the mass conservation (continuity) equation and is used to anticipate the form and evolution of the melt pool. Equation (4) is the energy conservation equation, which models heat conduction, melting, and solidification processes. Equation (5) corresponds to the momentum conservation equation and describes the velocity and flow behavior of the molten material within the melt pool.

$$\nabla \cdot \vec{v} = 0 \quad (3)$$

$$\rho \left[\frac{\partial}{\partial t} (\vec{v}) + \vec{v} \cdot \nabla \vec{v} \right] = -\vec{v} p + \nabla \cdot (\mu (\nabla \vec{v} + \nabla \vec{v}^T)) - \frac{2}{3} \delta_{ij} \nabla \cdot \vec{v} - \frac{C_1 (1 - f_l)^2}{C_2 + f_l^2} \vec{v} - \rho g \beta (T - T_l) \quad (4)$$

$$\frac{\partial h}{\partial t} + (\nabla \cdot \vec{v}) h = \frac{1}{\rho} (\nabla \cdot k \nabla T) \quad (5)$$

Where, ρ represent fluid density, \vec{v} show velocity vector of flow field, ∇ represent gradient operator, and p represent hydrodynamic pressure. μ represent the kinematic viscosity of the liquid, and δ_{ij} represent Kronecker delta. C_1 and C_2 are empirical constants of order of 10^6 and 10^{-4} respectively used for modeling solidification drag force [12]. f_l represent the drag force coefficient, g is gravitational acceleration, and β represent coefficient of thermal expansion. T represent the fluid temperature, while T_l denote the melting temperature. k denotes thermal conductivity, and h represent specific enthalpy.

2.3. Volume of fluid method

To predict and seize the free surface of the melt pool, Volume of Fluid (VOF) has been employed. VOF uses the mass, energy, and momentum conservation equations. Equation (6) represents the VOF method.

$$\frac{\partial V_f}{\partial t} + \nabla \cdot (\vec{v} \cdot V_f) = 0 \quad (6)$$

Where, V_f is fluid fraction within the computational cell and its minimum value of 0 represents no fluid, while $V_f = 1$ represent the cell is loaded with fluid. The surface of the fluid is represented for values other than 0 and 1 [13,14].

2.4. Particle size distribution

In the present work, a realistic particle size distribution was employed to model the LPBF process of IN718 powder. IN718 powder was received from Spirit AeroSystems. To characterize the powder morphology and size distribution, SEM (Tescan Vega3) was utilized. Figure 1 illustrates the particle size distribution of the IN718 powder. It can be observed that approximately 26 % of the powder particles are smaller than 10 μm , while about 64 % fall within the 10–30 μm range. This realistic particle size distribution was included in the simulation to precisely capture the melt pool behavior within the powder bed. The material properties of IN718 employed in the LPBF model are listed in Table 1.

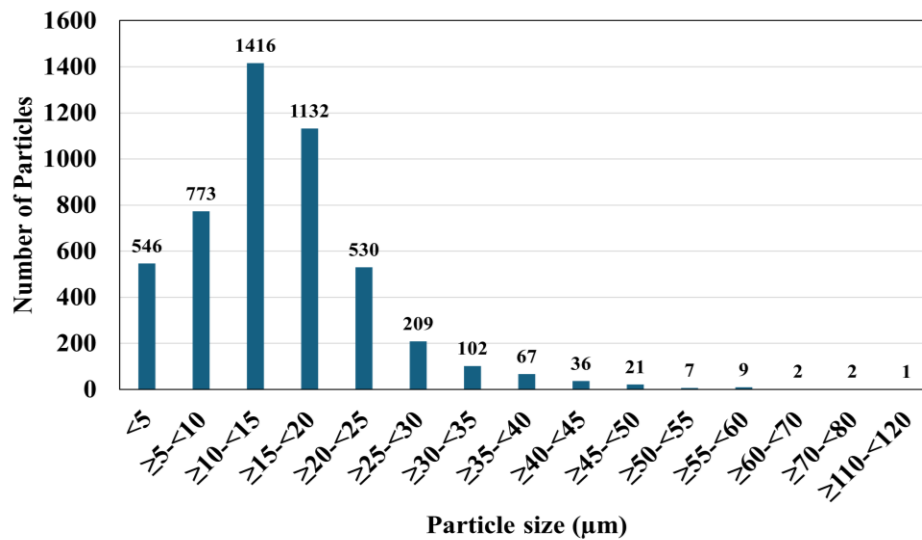


Figure 1: Particle size distribution of IN718 powder.

Table 1: Material properties of IN718 powder.

Property	Value
Solidus temperature T_s (K)	1523.15
Liquidus temperature T_l (K)	1608.15
Density ρ (kg/m^3)	5.96
Thermal conductivity k_1 ($\text{erg}/\text{cm}/\text{s}/\text{K}$)	2.9×10^6
Specific heat capacity c ($\text{erg}/\text{g}/\text{K}$)	7.2×10^6
Latent heat of fusion L (erg/g)	2.1×10^9
Surface tension coefficient σ (g/s^2)	1882
Temperature coefficient of surface tension $\frac{\partial \sigma}{\partial T}$ ($\text{g}/(\text{s}^2 \text{K})$)	0

2.5. 3D modeling of the circular cavity

FLOW-3D v12.0 (Flow Science, Inc., USA) has been employed in this study to simulate the single-track LPBF process of IN718. A rectangular substrate with dimensions of 1 mm × 1 mm × 0.6 mm in the X, Y, and Z directions, respectively, was modeled, featuring a circular cavity of 0.4 mm radius and 0.05 mm depth, as illustrated in Figure 2. Powder particles were deposited onto the substrate, filling the cavity. The boundary conditions implemented to the six faces of the computational domain are listed in Table 2. Subsequently, a recoating blade moved over the substrate at a velocity of 1.25 mm/s to remove excess powder from the surface. Table 3 summarizes the linear spring constants and friction coefficients used for particle modeling. After powder spreading, a 1000 W laser, traveling at a speed of 300 cm/s, was modeled to melt the settled powder bed.

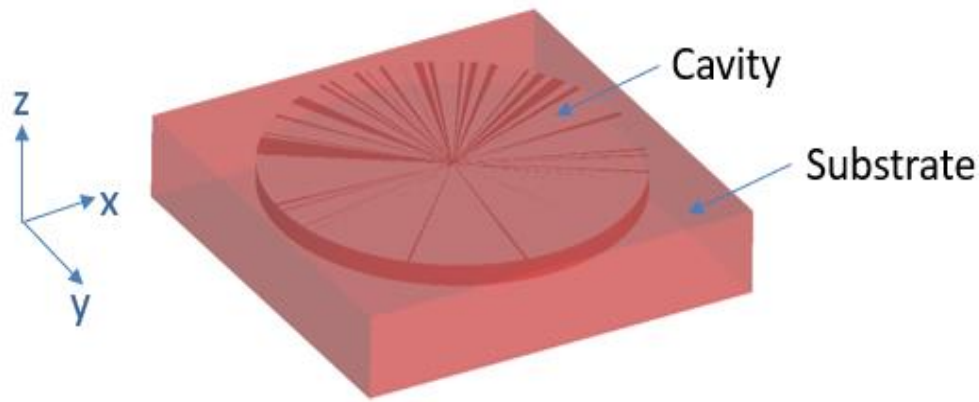


Figure 2: Illustration of the substrate with a circular cavity for the LPBF model.

Table 2: Boundary conditions used in the model.

Boundary	Condition
X min	Outflow
X max	Outflow
Y min	Wall
Y max	Wall
Z min	Symmetry
Z max	Pressure, 1 Pa

Table 3: Linear spring and friction coefficients used in DEM module.

Property	Value
Linear spring constant	20
Coefficient of restitution (normal direction)	0.3
Coefficient of restitution (tangential direction)	0.3
Particle static friction coefficient	0.2
Particle dynamic friction coefficient	0.15
Wall static friction coefficient	0.2
Wall dynamic friction coefficient	0.15

Results and Discussion

3.1. Melt pool characterization

Figure 3 (a) presents the top view of the melted track formed on the IN718 powder layer deposited over the circular substrate. The red-colored region defines the area melted by the laser. It can be perceived, at a laser power of 1000 W and a scan speed of 300 cm/s, the powder particles are completely melted. Figure 3 (b) presents a cross-section of the melt pool taken across the width of the melt track. The cross-section reveals a semi-elliptical melt pool shape, which is attributed to the Gaussian laser beam profile used in the simulation. The Gaussian profile delivers maximum energy density at the center of the beam, resulting in a deeper and narrower melted region at the center, thereby forming a semi-elliptical shape. The dimensions of the melt pool were extracted using FLOW-3D POST. The measured melt pool width is 136 μm , and the depth is 68.5 μm .

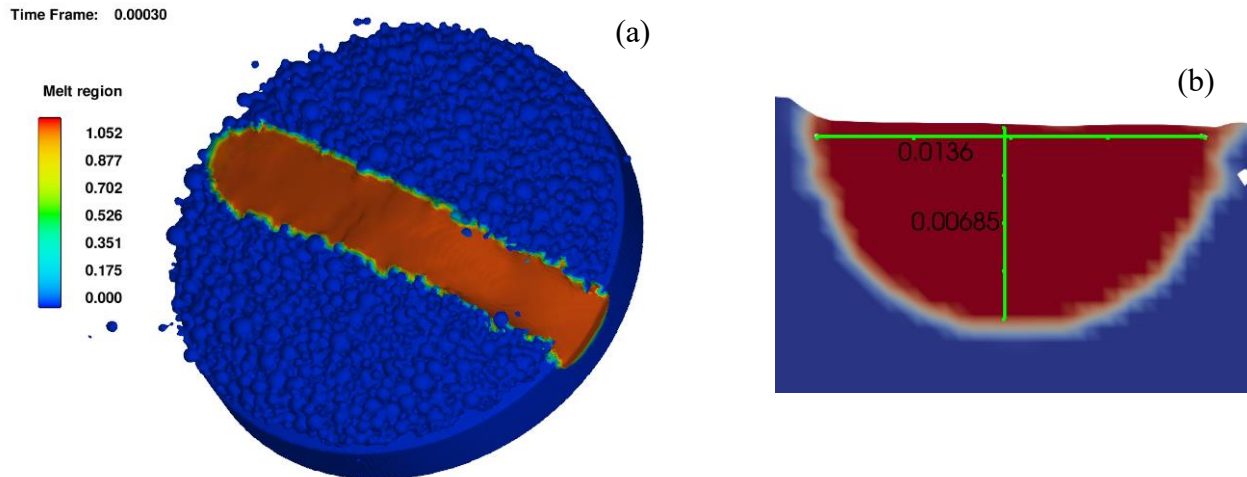


Figure 3: (a) Top view of melted powder bed, and (b) cross-sectional view of the melt pool.

3.2. Influence of airflow on powder bed

Airflow over the powder bed can cause non-uniformities and introduce defects during the melting process in LPBF. Figure 4 illustrates the schematic of the boundary conditions used to model the influence of airflow on the powder bed. The airflow is directed along the X-axis. The X-min boundary is defined as the velocity inlet for the incoming airflow. In contrast, the X-max boundary serves as the outlet, allowing particles that cross this boundary to be removed from the simulation domain. The remaining boundaries: Y-min, Y-max, Z-min, and Z-max are assigned to be same conditions as specified in Table 2.

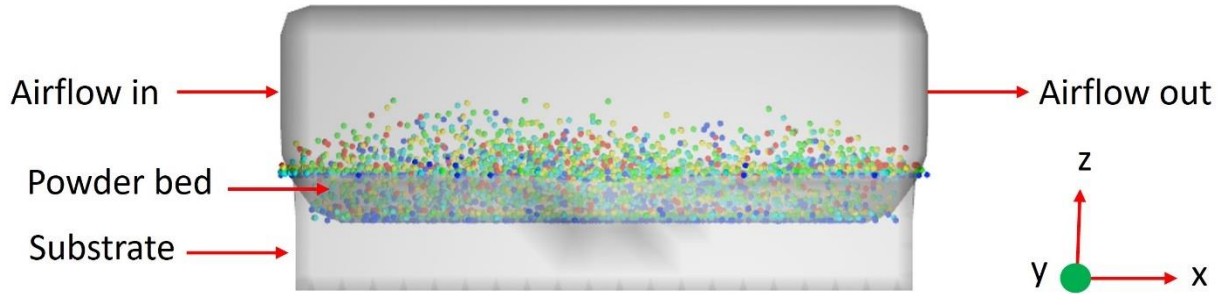


Figure 4: Modeling airflow effect on powder bed.

Two-way momentum coupling was enabled in the simulation to capture the interaction between powder particles and the surrounding airflow. Figure 5 depicts the ramification of airflow on the generated powder bed following the spreading process. Figure 5 (a) shows the powder bed without any airflow, where the particles are fully settled due to the absence of airflow. Figure 5 (b) shows the powder bed subjected to an airflow velocity of 8 cm/s, and Figure 5 (c) shows the case with a higher airflow velocity of 16 cm/s. As seen in Figures 5 (b) and 5 (c), some powder particles are lifted and appear suspended above the powder bed surface. This behavior indicates that the airflow displaces finer particles from the settled bed, with higher velocities resulting in greater particle displacement. These observations highlight the importance of airflow control in maintaining powder bed uniformity during LPBF process.

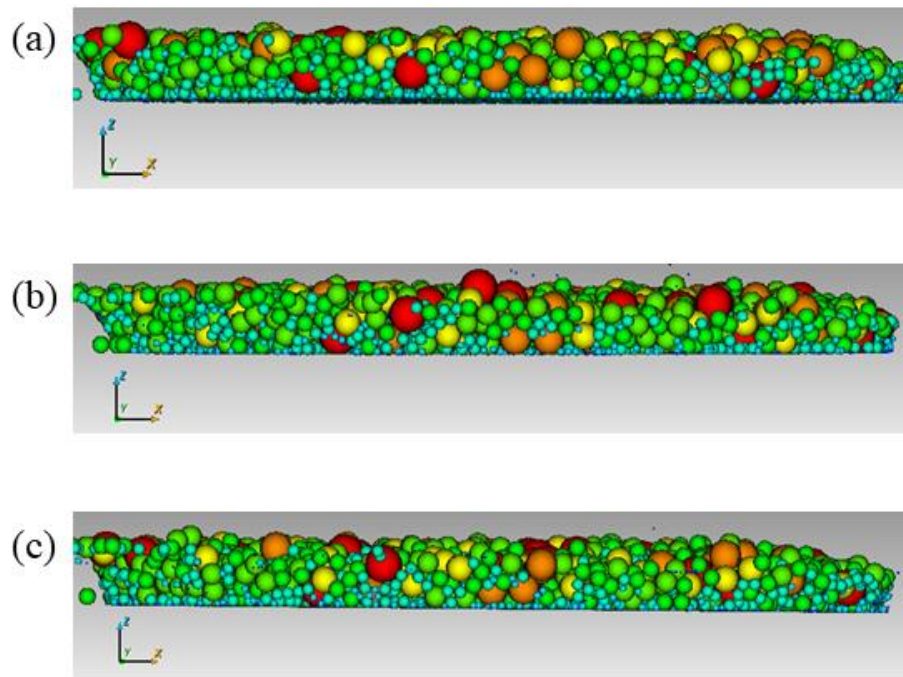


Figure 5: Powder bed (a) without airflow, (b) airflow at 8 cm/s, and (c) airflow at 16 cm/s.

In this study, six different cases were analyzed by varying the airflow velocity at 8 cm/s, 16 cm/s, 24 cm/s, 32 cm/s, 40 cm/s, and 48 cm/s. Table 4 summarizes the effect of airflow on the

powder bed at these velocities. Table 4 represents the number of powder particles removed from the bed in each case. The results signify that increasing the airflow velocity has a significant impact on powder bed stability. As the airflow velocity increases from 8 cm/s to 48 cm/s, the number of particles eliminated from the simulation domain rises substantially. This trend demonstrates that higher airflow intensifies particle entrainment, underscoring the importance of controlling airflow conditions in LPBF to maintain powder bed uniformity and reduce the risk of defect formation.

Table 4: Influence of airflow on the number of particles removed from the powder bed.

Airflow velocity	Powder particle size			
	2.5 microns	7.5 microns	12.5 microns	17.5 microns
8 cm/s	-	-	-	-
16 cm/s	-	-	-	-
24 cm/s	0.39%	1.07%	-	-
32 cm/s	1.35%	1.36%	1.12%	-
40 cm/s	1.84%	1.71%	1.32%	0.63%
48 cm/s	2.13%	2.07%	1.32%	1.01%

Conclusions

In this work, a multiphysics numerical model was developed to simulate the LPBF process for circular cavity modeling of IN718 powder. The DEM was employed to model powder particle interactions, while the VOF method was applied to capture the free surface dynamics of the melt pool. The particle size distribution and density of IN718 powder, characterized using SEM, were incorporated to generate a realistic powder bed. A combination of 1000 W laser power and 300 cm/s scan speed was adequate for complete melting of the IN718 powder layer. Furthermore, the impact of airflow on powder bed stability was investigated. The results showed that airflow significantly alters the powder bed configuration. At the lowest tested velocity of 8 cm/s, no particle ejection was observed. However, as the airflow velocity increased, the number of particles removed from the powder bed also increased. At 48 cm/s, approximately 2.13 % of the 2.5 μm powder particles were eliminated from the simulation domain, highlighting the sensitivity of fine particles to airflow in LPBF environments.

Acknowledgement

Support from the Center for Aerospace Manufacturing Technologies (CAMT) at Missouri University of Science and Technology is gratefully acknowledged.

References

- [1] Cao, L., Li, J., Hu, J., Liu, H., Wu, Y., and Zhou, Q., “Optimization of surface roughness and dimensional accuracy in LPBF additive manufacturing,” *Optics and Laser Technology*, Vol. 142, pp. 1–11, 2021. <https://doi.org/10.1016/j.optlastec.2021.107246>.
- [2] Weiss, C., Heslenfeld, J., Saewe, J.K., Bremen, S., and Häfner, C.L., “Investigation on the influence of powder humidity in Laser Powder Bed Fusion (LPBF),” *Procedia CIRP*, Vol. 111, pp. 115–120, 2022. <https://doi.org/10.1016/j.procir.2022.08.102>.
- [3] Simson, D., and Subbu, S.K., “Effect of process parameters on surface integrity of LPBF Ti6Al4V,” *Procedia CIRP*, Vol. 108, pp. 716–721, 2022. <https://doi.org/10.1016/j.procir.2022.03.111>.
- [4] Bartolomeis, A.D., Newman, S.T., Jawahir, I.S., Biermann, D., and Shokrani, A., “Future research directions in the machining of Inconel 718,” *Journal of Materials Processing Technology*, Vol. 297, pp. 1–21, 2021. <https://doi.org/10.1016/j.jmatprotec.2021.117260>.
- [5] Gruber, K., Smolina, I., Kasprowicz, M., and Kurzynowski, T., “Evaluation of inconel 718 metallic powder to optimize the reuse of powder and to improve the performance and sustainability of the laser powder bed fusion (LPBF) process,” *Materials*, Vol. 14, pp. 1–27, 2021. <https://doi.org/10.3390/ma14061538>.
- [6] Shrivastava, A., Kumar, S.A., Rao, S., and Nagesha, B.K., “Exploring how LPBF process parameters impact the interface characteristics of LPBF Inconel 718 deposited on Inconel 718 wrought substrates,” *Optics and Laser Technology*, Vol. 174, pp. 1–19, 2024. <https://doi.org/10.1016/j.optlastec.2024.110571>.
- [7] Sanchez, S., Rengasamy, D., Hyde, C.J., Figueredo, G.P., and Rothwell, B., “Machine learning to determine the main factors affecting creep rates in laser powder bed fusion,” *Journal of Intelligent Manufacturing*, Vol. 32, pp. 2353–2373, 2021. <https://doi.org/10.1007/s10845-021-01785-0>.
- [8] Wang, Q., Michaleris, P., Pantano, M., Li, C., Ren, Y., and Nassar, A.R., “Part-scale thermal evolution and post-process distortion of Inconel-718 builds fabricated by laser powder bed fusion,” *Journal of Manufacturing Processes*, Vol. 81, pp. 865–880, 2022. <https://doi.org/10.1016/j.jmapro.2022.07.026>.
- [9] Pramod, S., and Kesavan, D., “Melting modes of laser powder bed fusion (L-PBF) processed IN718 alloy: Prediction and experimental analysis,” *Advances in Industrial and Manufacturing Engineering*, Vol. 6, pp. 1–17, 2023. <https://doi.org/10.1016/j.aime.2022.100106>.
- [10] An, Z., Pan, J., Hu, X., and Yang, H., “Analysis of melt pool evolution, defect mechanisms, and grain growth of Inconel 625 formers in selective laser melting,”

International Journal of Heat and Mass Transfer, Vol. 238, pp. 1–14, 2025.
<https://doi.org/10.1016/j.ijheatmasstransfer.2024.126452>.

- [11] Dai, L., Wu, J., Li, L., Meng, X., Zhang, H., Li, P., Huang, S., and Zhou, J., “A discrete element model for analyzing porosity defect evolution in multi-layer laser powder bed fusion of 2195 Al-Li alloy,” *Journal of Alloys and Compounds*, Vol. 1036, pp. 1–13, 2025.
<https://doi.org/10.1016/j.jallcom.2025.181689>.
- [12] Alphonso, W.E., Baier, M., Carmignato, S., Hattel, J.H., and Bayat, M., “On the possibility of doing reduced order, thermo-fluid modelling of laser powder bed fusion (L-PBF) – Assessment of the importance of recoil pressure and surface tension,” *Journal of Manufacturing Processes*, Vol. 94, pp. 564–577, 2023.
<https://doi.org/10.1016/j.jmapro.2023.03.040>.
- [13] Rangapuram, M., Yang, M., Babalola, S., Newkirk, J.W., Bartlett, L.N., Liou, F.F., and Chandrashekhara, K., “A multiphysics modeling approach to assess the powder bed characteristics of high strength steel in selective laser melting,” in: *Solid Freeform Fabrication 2022: Proceedings of the 33rd Annual International Solid Freeform Fabrication Symposium – An Additive Manufacturing Conference*, pp. 1–13.
<https://doi.org/doi.org/10.26153/tsw/44577>.
- [14] Rangapuram, M., Babalola, S., Newkirk, J.W., Bartlett, L.N., Liou, F.W., Chandrashekhara, K., and Cluff, S.R., “Multiphysics modeling and experimental validation of high-strength steel in laser powder bed fusion process,” *Progress in Additive Manufacturing*, Vol. 9, pp. 1697–1713, 2023. <https://doi.org/10.1007/s40964-023-00532-6>.